

1

2 The ANTsX Ecosystem for Mapping the 3 Mouse Brain

4 Nicholas J. Tustison¹, Min Chen², Fae N. Kronman³, Jeffrey T. Duda², Clare Gamlin⁴, Mia
5 G. Tustison, Michael Kunst⁴, Rachel Dalley⁴, Staci Sorenson⁴, Quanxi Wang⁴, Lydia Ng⁴,
6 Yongsoo Kim³, and James C. Gee²

7 ¹Department of Radiology and Medical Imaging, University of Virginia, Charlottesville, VA

8 ²Department of Radiology, University of Pennsylvania, Philadelphia, PA

9 ³Department of Neural and Behavioral Sciences, Penn State University, Hershey, PA

10 ⁴Allen Institute for Brain Science, Seattle, WA

11 _____

12 Corresponding authors:

13

14 Nicholas J. Tustison, DSc

15 Department of Radiology and Medical Imaging

16 University of Virginia

17 ntustison@virginia.edu

18

19 James C. Gee, PhD

20 Department of Radiology

21 University of Pennsylvania

22 gee@upenn.edu

²³ **Abstract**

²⁴ Precision mapping techniques coupled with high resolution image acquisition of the mouse
²⁵ brain permit the study of the spatial organization of gene expression and their mutual in-
²⁶ teraction for a comprehensive view of salient structural/functional relationships. Such re-
²⁷ search is facilitated by standardized anatomical coordinate systems, such as the well-known
²⁸ Allen Common Coordinate Framework (AllenCCFv3), and the ability to spatially map to
²⁹ such standardized spaces. The Advanced Normalization Tools Ecosystem is a comprehen-
³⁰ sive open-source software toolkit for generalized quantitative imaging with applicability to
³¹ multiple organ systems, modalities, and animal species. Herein, we illustrate the utility
³² of ANTsX for generating precision spatial mappings of the mouse brain and potential sub-
³³ sequent quantitation. We describe ANTsX-based workflows for mapping domain-specific
³⁴ image data to AllenCCFv3 accounting for common artefacts and other confounds. Novel
³⁵ contributions include ANTsX functionality for velocity flow-based mapping spanning the
³⁶ spatiotemporal domain of a longitudinal trajectory which we apply to the Developmental
³⁷ Common Coordinate Framework. Additionally, we present an automated structural morpho-
³⁸ logical pipeline for determining volumetric and cortical thickness measurements analogous to
³⁹ the well-utilized ANTsX pipeline for human neuroanatomical structural morphology which
⁴⁰ illustrates a general open-source framework for tailored brain parcellations.

41 1 Introduction

42 Over the past two decades there have been significant advancements in mesoscopic analysis
43 of the mouse brain. It is currently possible to track single cell neurons in mouse brains,¹
44 observe whole brain developmental changes on a cellular level,² associate brain regions and
45 tissues with their genetic composition,³ and locally characterize neural connectivity.⁴ Much
46 of this scientific achievement has been made possible due to breakthroughs in high resolution
47 imaging techniques that permit submicron, 3-D imaging of whole mouse brains. Associated
48 research techniques such as micro-optical sectioning tomography,⁶ tissue clearing,^{1,7} spatial
49 transcriptomics⁹ are all well-utilized in the course of scientific investigations of mesoscale
50 relationships in the mouse brain.

51 An important component of this research is the ability to map the various image data to
52 anatomical reference frames¹¹ for inferring spatial relationships between structures, cells,
53 and genetics. This has motivated the development of detailed structural image atlases of
54 the mouse brain. Notable examples include the Allen Brain Atlas and Common Coordinate
55 Frameworks (AllenCCFv3),¹³ the Waxholm Space,¹⁴ and more recently, the Developmental
56 Common Coordinate Framework (DevCCF).¹⁵ Despite the significance of these contribu-
57 tions, challenges still exist in large part due to the wide heterogeneity in associated study-
58 specific image data. For example, variance in the acquisition methods can introduce artifacts
59 such as tissue distortion, holes, bubbles, folding, tears, and missing slices. These complicate
60 assumed correspondence for conventional spatial mapping approaches.

61 1.1 Mouse-specific brain mapping software

62 To address such challenges, several software packages have been developed over the years
63 comprising solutions of varying comprehensibility, sophistication, and availability. An
64 early contribution to the community was the Rapid Automatic Tissue Segmentation
65 (RATS) package¹⁶ for brain extraction. More recently, several publicly available packages
66 comprise well-established package dependencies originally developed on human brain data.
67 SPMMouse,¹⁷ for example, is based on the well-known Statistical Parametric Mapping

68 (SPM) Matlab-based toolset.¹⁸ The automated mouse atlas propagation (aMAP) tool is
69 largely a front-end for the NiftyReg image registration package¹⁹ applied to mouse data
70 which is currently available as a Python module.²⁰ NiftyReg is also used by the Atlas-based
71 Imaging Data Analysis (AIDA) MRI pipeline²¹ as well as the Multi Atlas Segmentation
72 and Morphometric Analysis Toolkit (MASMAT). Whereas the former also incorporates the
73 FMRIB Software Library (FSL)²² for brain extraction and DSISTudio²³ for DTI processing,
74 the latter uses NiftySeg and multi-consensus labeling tools²⁴ for brain extraction and
75 parcellation. In addition, MASMAT incorporates N4 bias field correction²⁵ from the Ad-
76 vanced Normalization Tools Ecosystem (ANTsX)²⁶ as do the packages Multi-modal Image
77 Registration And Connectivity anaLysis (MIRACL),²⁷ Saamba-MRI,²⁸ and Small Animal
78 Magnetic Resonance Imaging (SAMRI).²⁹ However, whereas Saamba-MRI uses AFNI³⁰
79 for image registration; MIRACL, SAMRI, SAMBA,³¹ and BrainsMapi³² all use ANTsX
80 registration tools. Other packages use landmark-based approaches to image registration
81 including SMART—³³an R package for semi-automated landmark-based registration and
82 segmentation of mouse brain based on WholeBrain.³⁴ Relatedly, FriendlyClearMap³⁵ and
83 mBrainAligner³⁶ are both landmark-based approaches to mapping of the mouse brain.
84 Whereas the former employs Elastix³⁷ functionality, the latter is based on developed
85 methodology referred to as *coherent landmark mapping*. Finally, the widespread adoption
86 of deep learning techniques has also influenced development in mouse brain imaging
87 methodologies. For example, if tissue deformations are not considered problematic for a
88 particular dataset, DeepSlice can be used to determine affine mappings³⁸ with the optimal
89 computational efficiency associated with neural networks.

90 1.2 The ANTsX Ecosystem for mouse brain mapping

91 As noted previously, many of the existing packages designed for processing mouse brain image
92 data use ANTsX tools for core processing steps in various workflows, particularly its pair-
93 wise, intensity-based image registration capabilities and bias field correction. Historically,
94 ANTsX development is originally based on fundamental approaches to image mapping,^{39–41}
95 particularly in the human brain, which has resulted in core contributions to the field such as

Table 1: Sampling of ANTsX functionality

<i>ANTsPy: Preprocessing</i>	
bias field correction	<code>n4_bias_field_correction(...)</code>
image denoising	<code>denoise_image(...)</code>
<i>ANTsPy: Registration</i>	
image registration	<code>registration(...)</code>
image transformation	<code>apply_transforms(...)</code>
template generation	<code>build_template(...)</code>
landmark registration	<code>fit_transform_to_paired_points(...)</code>
time-varying landmark reg.	<code>fit_time_varying_transform_to_point_sets(...)</code>
integrate velocity field	<code>integrate_velocity_field(...)</code>
invert displacement field	<code>invert_displacement_field(...)</code>
<i>ANTsPy: Segmentation</i>	
MRF-based segmentation	<code>atropos(...)</code>
Joint label fusion	<code>joint_label_fusion(...)</code>
diffeomorphic thickness	<code>kelly_kapowski(...)</code>
<i>ANTsPy: Miscellaneous</i>	
Regional intensity statistics	<code>label_stats(...)</code>
Regional shape measures	<code>label_geometry_measures(...)</code>
B-spline approximation	<code>fit_bspline_object_to_scattered_data(...)</code>
Visualize images and overlays	<code>plot(...)</code>
<i>ANTsPyNet: Mouse-specific</i>	
brain extraction	<code>mouse_brain_extraction(...modality="t2"...)</code> <code>mouse_brain_extraction(...modality="ex5"...)</code>
brain parcellation	<code>mouse_brain_parcellation(...)</code>
cortical thickness	<code>mouse_cortical_thickness(...)</code>
super resolution	<code>mouse_histology_super_resolution(...)</code>

ANTsX provides state-of-the-art functionality for processing biomedical image data. Such tools, including deep learning networks, support a variety of mapping-related tasks. A more comprehensive listing of ANTsX tools with self-contained R and Python examples is provided as a gist page on GitHub (<https://tinyurl.com/antsxtutorial>).

the well-known Symmetric Normalization (SyN) algorithm.⁴² Since its development, various independent platforms have been used to evaluate ANTsX image registration capabilities in the context of different application foci which include multi-site brain MRI data,⁴³ pulmonary CT data,⁴⁴ and most recently, multi-modal brain registration in the presence of tumors.⁴⁵

Apart from its registration capabilities, ANTsX comprises additional functionality such as template generation,⁴⁶ intensity-based segmentation,⁴⁷ preprocessing,^{25,48} deep learning networks,²⁶ and other miscellaneous utilities (see Table 1). The comprehensive use of the toolkit has demonstrated superb performance in multiple application areas (e.g., consensus labeling,⁴⁹ brain tumor segmentation,⁵⁰ and cardiac motion estimation⁵¹). Importantly, ANTs is built on the Insight Toolkit (ITK)⁵² deriving benefit from the open-source community of scientists and programmers as well as providing an important resource for algorithmic development, evaluation, and improvement. We use this functionality to demonstrate recently developed frameworks for mapping fluorescence micro-optical sectioning tomography (fMOST) and multiplexed error-robust fluorescence *in situ* hybridization (MERFISH) image data to the AllenCCFv3 atlas space. In addition to standard preprocessing steps (e.g., bias correction), additional considerations are accommodated within the ANTsX ecosystem, such as section reconstruction and landmark-based alignment with corresponding processing scripts available at <https://github.com/dontminchenit/CCFAAlignmentToolkit>.

1.3 ANTsX-based open-source contributions

Consistent with previous ANTsX development, the newly introduced capabilities introduced below are available through ANTsX (specifically, via R and Python ANTsX packages), and illustrated through self-contained examples in the ANTsX tutorial (<https://tinyurl.com/antsxtutorial>) with a dedicated GitHub repository specific to this work (<https://github.com/ntustison/ANTsXMouseBrainMapping>).

¹²¹ **1.3.1 The DevCCF velocity flow model**

¹²² Recently, the Developmental Common Coordinate Framework (DevCCF) was introduced to
¹²³ the mouse brain research community as a public resource¹⁵ comprising symmetric atlases
¹²⁴ of multimodal image data and anatomical segmentations defined by developmental ontol-
¹²⁵ ogy. These templates sample the mouse embryonic days (E) 11.5, E13.5, E15.5, E18.5 and
¹²⁶ postnatal day (P) 4, P14, and P56. Modalities include light sheet fluorescence microscopy
¹²⁷ (LSFM) and at least four MRI contrasts per developmental stage. Anatomical parcellations
¹²⁸ are also available for each time point and were generated from ANTsX-based mappings of
¹²⁹ gene expression and other cell type data. Additionally, the P56 template was integrated
¹³⁰ with the AllenCCFv3 to further enhance the practical utility of the DevCCF. These pro-
¹³¹ cesses, specifically template generation and multi-modal image mapping, were performed
¹³² using ANTsX functionality in the presence of image mapping difficulties such as missing
¹³³ data and tissue distortion.¹⁵

¹³⁴ Given the temporal gaps in the discrete set of developmental atlases, we also provide an
¹³⁵ open-source framework for inferring correspondence within the temporally continuous do-
¹³⁶ main sampled by the existing set of embryonic and postnatal atlases of the DevCCF. This
¹³⁷ recently developed functionality permits the generation of a diffeomorphic velocity flow trans-
¹³⁸ formation model,⁵³ influenced by previous work.⁵⁴ The resulting time-parameterized velocity
¹³⁹ field spans the stages of the DevCCF where mappings between any two continuous time
¹⁴⁰ points within the span bounded by the E11.5 and P56 atlases is determined by integration
¹⁴¹ of the optimized velocity field.

¹⁴² **1.3.2 Structural morphology and cortical thickness in the mouse brain**

¹⁴³ One of the most frequently utilized pipelines in the ANTsX toolkit is that of estimating corti-
¹⁴⁴ cal thickness maps in the human brain. Beginning with the Diffeomorphic Registration-based
¹⁴⁵ Cortical Thickness (DiReCT) algorithm,⁵⁵ this was later expanded to include a complete pro-
¹⁴⁶ cessing framework for human brain cortical thickness estimation for both cross-sectional⁵⁶
¹⁴⁷ and longitudinal⁵⁷ data using T1-weighted MRI. These pipelines were later significantly

¹⁴⁸ refactored using deep learning innovations.²⁶

¹⁴⁹ In contrast to the pipeline development in human data,²⁶ no current ANTsX tools exist to
¹⁵⁰ create adequate training data for the mouse brain. In addition, mouse brain data acquisition
¹⁵¹ often has unique issues, such as lower data quality or sampling anisotropy which limits
¹⁵² its applicability to high resolution resources (e.g., AllenCCFv3, DevCCF), specifically with
¹⁵³ respect to the corresponding granular brain parcellations derived from numerous hours of
¹⁵⁴ expert annotation leveraging multimodal imaging resources.

¹⁵⁵ Herein, we introduce a mouse brain cortical thickness pipeline for T2-weighted (T2-w) MRI
¹⁵⁶ comprising two novel deep learning components: two-shot learning brain extraction from
¹⁵⁷ data augmentation of two ANTsX templates generated from two open datasets^{58,59} and
¹⁵⁸ single-shot brain parcellation derived from the AllenCCFv3 labelings mapped to the corre-
¹⁵⁹ sponding DevCCF P56 T2-w component. Although we anticipate that this cortical thickness
¹⁶⁰ pipeline will be beneficial to the research community, this work demonstrates more generally
¹⁶¹ how one can leverage ANTsX tools for developing tailored brain parcellation schemes using
¹⁶² these publicly available resources. Evaluation is performed on an independent open dataset⁶⁰
¹⁶³ comprising longitudinal acquisitions of multiple specimens.

164 **2 Results**

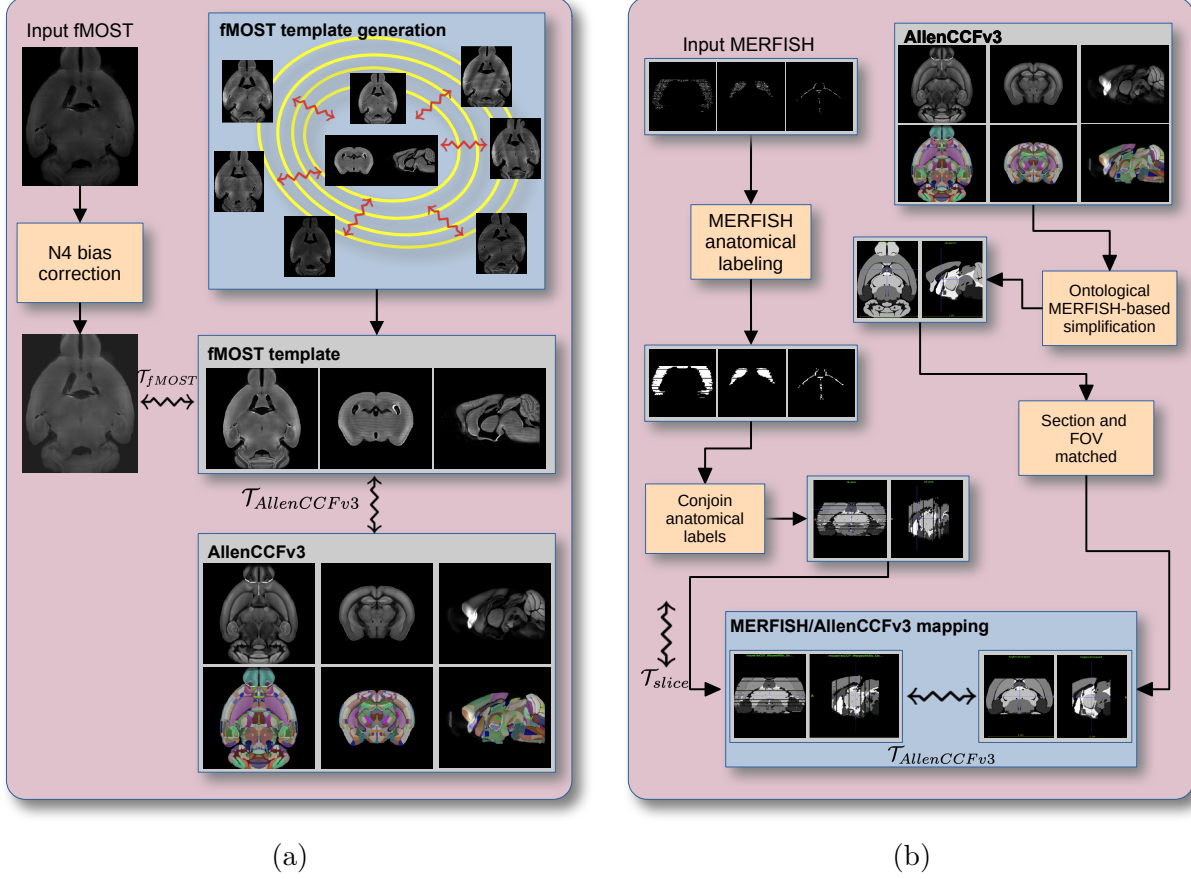


Figure 1: Diagrammatic illustration of the two ANTsX-based pipelines for mapping (a) fMOST and (b) MERFISH data into the space of AllenCCFv3. Each generates the requisite transforms, \mathcal{T} , to map individual images.

165 **2.1 AllenCCFv3 brain image mapping**

166 **2.1.1 Mapping fluorescence micro-optical sectioning tomography data**

167 **Overview.** A framework for mapping fluorescence micro-optical sectioning tomography
 168 (fMOST) mouse brain images into the AllenCCFv3 was developed (see Figure 1(a)). An
 169 intensity- and shape-based average fMOST atlas serves as an intermediate registration target
 170 for mapping fMOST images from individual specimens into the AllenCCFv3. Preprocess-
 171 ing steps include downsampling to match the $25\mu m$ isotropic AllenCCFv3, acquisition-based

172 stripe artifact removal, and inhomogeneity correction.²⁵ Preprocessing also includes a single
173 annotation-driven registration to establish a canonical mapping between the fMOST atlas
174 and the AllenCCFv3. This step allows us to align expert determined landmarks to accu-
175 rately map structures with large morphological differences between the modalities, which are
176 difficult to address using standard approaches. Once this canonical mapping is established,
177 standard intensity-based registration is used to align each new fMOST image to the fMOST
178 specific atlas. This mapping is concatenated with the canonical fMOST atlas-to-AllenCCFv3
179 mapping to further map each individual brain into the latter without the need to generate
180 additional landmarks. Transformations learned through this mapping can be applied to sin-
181 gle neuron reconstructions from the fMOST images to evaluate neuronal distributions across
182 different specimens into the AllenCCFv3 for the purpose of cell census analyses.

183 **Data.** The high-throughput and high-resolution fluorescence micro-optical sectioning to-
184 mography (fMOST)^{61,62} platform was used to image 55 mouse brains containing gene-defined
185 neuron populations, with sparse transgenic expression.^{63,64} In short, the fMOST imaging
186 platform results in 3-D images with voxel sizes of $0.35 \times 0.35 \times 1.0 \mu\text{m}^3$ and is a two-channel
187 imaging system where the green channel displays the green fluorescent protein (GFP) labeled
188 neuron morphology and the red channel is used to visualize the counterstained propidium
189 iodide cytoarchitecture. The spatial normalizations described in this work were performed
190 using the red channel, which offered higher tissue contrast for alignment, although other
191 approaches are possible including multi-channel registration.

192 **Evaluation.** Evaluation of the canonical fMOST atlas to Allen CCFv3 mapping was per-
193 formed via quantitative comparison at each step of the registration and qualitative assess-
194 ment of structural correspondence after alignment by an expert anatomist. Dice values were
195 generated for the following structures: whole brain, 0.99; fimbria, 0.91; habenular com-
196 missure, 0.63; posterior choroid plexus, 0.93; anterior choroid plexus, 0.96; optic chiasm,
197 0.77; caudate putamen, 0.97. Similar qualitative assessment was performed for each fMOST
198 specimen including the corresponding neuron reconstruction data.

199 **2.1.2 Mapping multiplexed error-robust fluorescence in situ hybridization**
200 **(MERFISH) data**

201 **Overview.** The unique aspects of mapping multiplexed error-robust fluorescence in situ
202 hybridization (MERFISH) spatial transcriptomic data onto AllenCCFv3⁶⁵ required the de-
203velopment of a separate ANTsX-based pipeline (see Figure 1(b)). Mappings are performed
204 by matching gene expression derived region labels from the MERFISH data to corresponding
205 anatomical parcellations of the AllenCCFv3. The pipeline consists of MERFISH data spe-
206cific preprocessing which includes section reconstruction, mapping corresponding anatomical
207 labels between AllenCCFv3 and the spatial transcriptomic maps of the MERFISH data, and
208 matching MERFISH sections to the atlas space. Following pre-processing, two main align-
209ment steps were performed: 1) 3-D global affine mapping and section matching of the Al-
210lenCCFv3 into the MERFISH data and 2) 2D global and deformable mapping between each
211MERFISH section and matched AllenCCFv3 section. Mappings learned via each step in the
212pipeline are preserved and concatenated to provide point-to-point correspondence between
213the original MERFISH data and AllenCCFv3, thus allowing individual gene expressions to
214be transferred into the AllenCCFv3.

215 **Data.** MERFISH mouse brain data was acquired using a previously detailed procedure.⁶⁵
216 Briefly, a brain of C57BL/6 mouse was dissected according to standard procedures and
217placed into an optimal cutting temperature (OCT) compound (Sakura FineTek 4583) in
218which it was stored at -80°C. The fresh frozen brain was sectioned at 10 μm on Leica 3050
219S cryostats at intervals of 200 μm to evenly cover the brain. A set of 500 genes were imaged
220that had been carefully chosen to distinguish the ~ 5200 clusters of our existing RNAseq
221taxonomy. For staining the tissue with MERFISH probes, a modified version of instructions
222provided by the manufacturer was used.⁶⁵ Raw MERSCOPE data were decoded using Vizgen
223software (v231). Cell segmentation was performed.⁶⁶ In brief, cells were segmented based
224on DAPI and PolyT staining using Cellpose.⁶⁷ Segmentation was performed on a median
225z-plane (fourth out of seven) and cell borders were propagated to z-planes above and below.
226 To assign cluster identity to each cell in the MERFISH dataset, we mapped the MERFISH
227cells to the scRNA-seq reference taxonomy.

228 **Evaluation.** Alignment of the MERFISH data into the AllenCCFv3 was qualitatively as-
229 sessed by an expert anatomist at each iteration of the registration using known correspon-
230 dence of gene markers and their associations with the AllenCCFv3. As previously reported,⁶⁵
231 further assessment of the alignment showed that, of the 554 terminal regions (gray matter
232 only) in the AllenCCFv3, only seven small subregions were missed from the MERFISH
233 dataset: frontal pole, layer 1 (FRP1), FRP2/3, FRP5; accessory olfactory bulb, glomerular
234 layer (AOBgl); accessory olfactory bulb, granular layer (AOBgr); accessory olfactory bulb,
235 mitral layer (AOBmi); and accessory supraoptic group (ASO).

236 **2.2 The DevCCF velocity flow model**

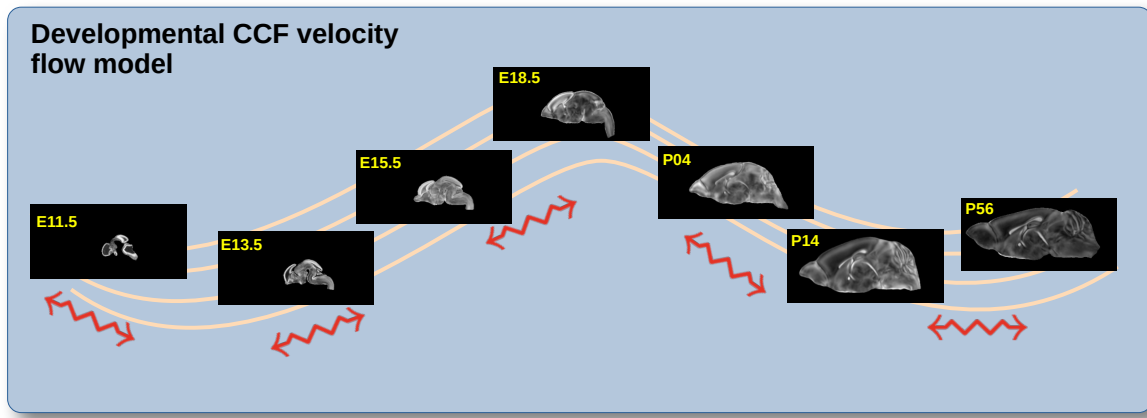


Figure 2: The spatial transformation between any two time points within the DevCCF longitudinal developmental trajectory is available through the use of ANTsX functionality for generating a velocity flow model.

237 To continuously interpolate transformations between the different stages of the DevCCF
238 atlases, a velocity flow model was constructed using DevCCF derived data and functionality
239 recently introduced into both the ANTsR and ANTsPy packages. Both platforms include
240 a complete suite of functions for determining dense correspondence from sparse landmarks
241 based on a variety of transformation models ranging from standard linear models (i.e., rigid,
242 affine) to deformable diffeomorphic models (e.g, symmetric normalization).⁴² The latter set
243 includes transformation models for both the pairwise scenario and for multiple sets, as in the

²⁴⁴ case of the DevCCF. ANTsX, being built on top of ITK, uses an ITK image data structure
²⁴⁵ for the 4-D velocity field where each voxel contains the x , y , z components of the field at
²⁴⁶ that point.

²⁴⁷ **2.2.1 Data**

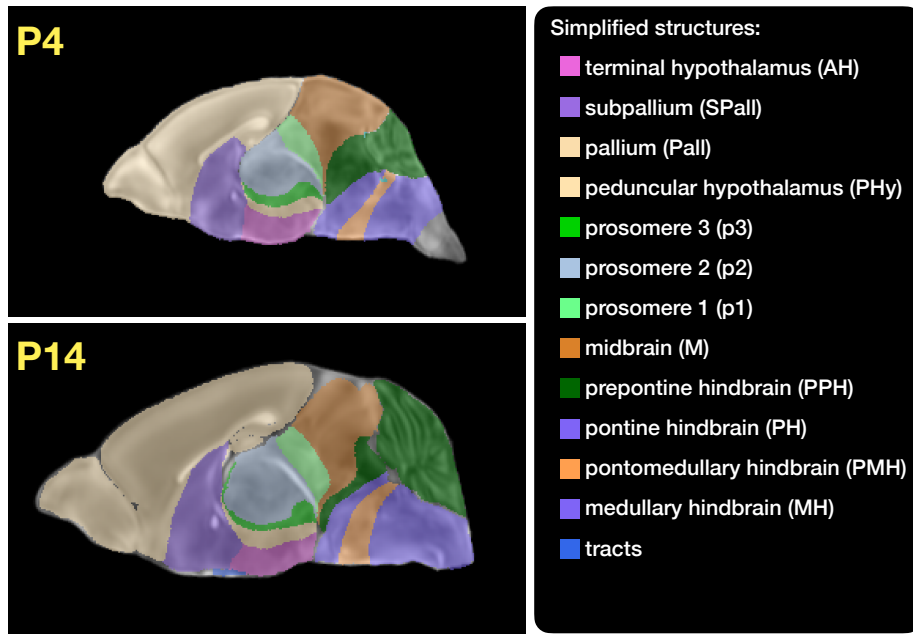


Figure 3: Annotated regions representing common labels across developmental stages which are illustrated for both P4 and P14.

²⁴⁸ Labeled annotations are available as part of the original DevCCF and reside in the space
²⁴⁹ of each developmental template which range in resolution from $31.5 - 50\mu\text{m}$. Across all
²⁵⁰ atlases, the total number of labeled regions exceeds 2500. From these labels, a common set
²⁵¹ of 26 labels (13 per hemisphere) across all atlases were used for optimization and evaluation.

²⁵² These simplified regions include: terminal hypothalamus, subpallium, pallium, peduncular
²⁵³ hypothalamus, prosomere, prosomere, prosomere, midbrain, prepontine hindbrain, pontine
²⁵⁴ hindbrain, pontomedullary hindbrain, medullary hindbrain, and tracts (see Figure 3).

²⁵⁵ Prior to velocity field optimization, all data were rigidly transformed to DevCCF P56 using
²⁵⁶ the centroids of the common label sets. In order to determine the landmark correspondence
²⁵⁷ across DevCCF stages, the multi-metric capabilities of `ants.registration(...)` were used.

258 Instead of performing intensity-based pairwise registration directly on these multi-label im-
 259 ages, each label was used to construct a separate fixed and moving image pair resulting in a
 260 multi-metric registration optimization scenario involving 24 binary image pairs (each label
 261 weighted equally) for optimizing diffeomorphic correspondence between neighboring time
 262 point atlases using the mean squares metric and the symmetric normalization transform.⁴²
 263 To generate the set of common point sets across all seven developmental atlases, the label
 264 boundaries and whole regions were sampled in the P56 atlas and then propagated to each
 265 atlas using the transformations derived from the pairwise registrations. We selected a sam-
 266 pling rate of 10% for the contour points and 1% for the regional points for a total number
 267 of points being per atlas being 173303 ($N_{contour} = 98151$ and $N_{region} = 75152$). Regional
 268 boundary points were weighted twice as those of non-boundary points during optimization.

269 2.2.2 Optimization

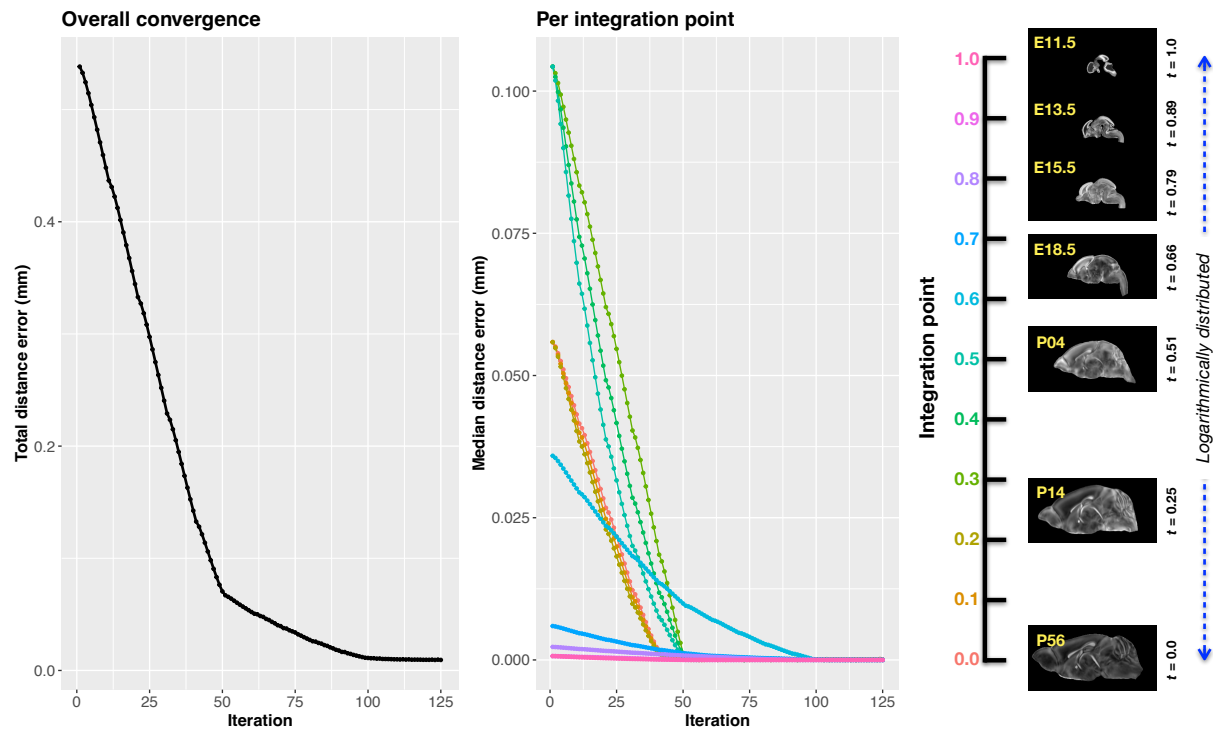


Figure 4: Convergence of the optimization of the velocity field for describing the transformation through the developmental stages from E11.5 through P56. Integration points in diagram on the right are color-coordinated with the center plot and placed in relation to the logarithmically situated temporal placement of the individual DevCCF atlases.

270 The velocity field was optimized using the input composed of the seven corresponding point
271 sets and their associated weight values, the selected number of integration points for the
272 velocity field ($N = 11$), and the parameters defining the geometry of the spatial dimensions
273 of the velocity field. Thus, the optimized velocity field described here is of size [256, 182, 360]
274 (50 μm isotropic) $\times 11$ integration points for a total compressed size of a little over 2 GB.
275 This choice represented weighing the trade-off between tractability, portability, and accuracy.
276 However, all data and code to reproduce the results described (with possible variation in the
277 input parameters) are available in the dedicated GitHub repository.

278 The normalized time point scalar value for each atlas/point-set in the temporal domains [0, 1]
279 was also defined. Given the increasingly larger gaps in the postnatal timepoint sampling, we
280 made two adjustments. Based on known mouse brain development, we used 28 days for the
281 P56 data. We then computed the log transform of the adjusted set of time points prior to
282 normalization between 0 and 1 (see the right side of Figure 4). This log transform, as part
283 of the temporal normalization, significantly improved data spacing.

284 The maximum number of iterations was set to 200 with each iteration taking approximately
285 six minutes on a 2020 iMac (processor, 3.6 GHz 10-Core Intel Core i9; memory, 64 GB 2667
286 MHz DDR4) At each iteration we looped over the 11 integration points. At each integration
287 point, the velocity field estimate was updated by warping the two immediately adjacent
288 point sets to the integration time point and determining the regularized displacement field
289 between the two warped point sets. As with any gradient-based descent algorithm, this field
290 was multiplied by a small step size ($\delta = 0.2$) before adding to the current velocity field.
291 Convergence is determined by the average displacement error over each of the integration
292 points. As can be seen in the left panel of Figure 4, convergence occurred around 125
293 iterations when the average displacement error over all integration points is minimized. The
294 median displacement error at each of the integration points also trends towards zero but at
295 different rates.

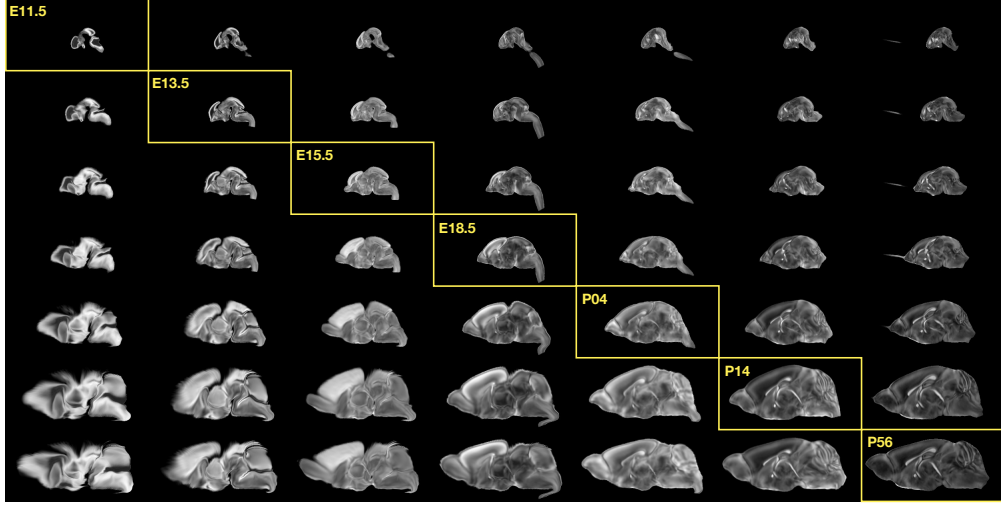


Figure 5: Mid-sagittal visualization of the effects of the transformation model in warping every developmental stage to the time point of every other developmental stage. The original images are located along the diagonal. Columns correspond to the warped original image whereas the rows represent the reference space to which each image is warped.

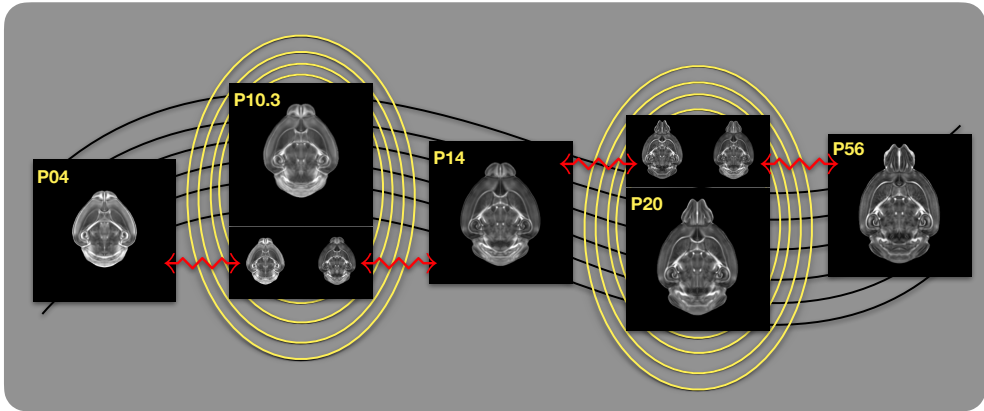


Figure 6: Illustration of the use of the velocity flow model for creating virtual templates at continuous time points not represented in one of the existing DevCCF time points. For example, FA templates at time point P10.3 and P20 can be generated by warping the existing temporally adjacent developmental templates to the target time point and using those images in the ANTsX template building process.

²⁹⁶ 2.2.3 The transformation model

²⁹⁷ Once optimized, the resulting velocity field can be used to generate the deformable transform
²⁹⁸ between any two continuous points within the time interval bounded by E11.5 and P56. In
²⁹⁹ Figure 5, we transform each atlas to the space of every other atlas using the DevCCF
³⁰⁰ transform model. Additionally, one can use this transformation model to construct virtual

301 templates in the temporal gaps of the DevCCF. Given an arbitrarily chosen time point
 302 within the normalized time point interval, the existing adjacent DevCCF atlases on either
 303 chronological side can be warped to the desired time point. A subsequent call to one of
 304 the ANTsX template building functions then permits the construction of the template at
 305 that time point. In Figure 6, we illustrate the use of the DevCCF velocity flow model for
 306 generating two such virtual templates for two arbitrary time points. Note that both of these
 307 usage examples can be found in the GitHub repository previously given.

308 2.3 The Mouse Cortical Thickness Pipeline

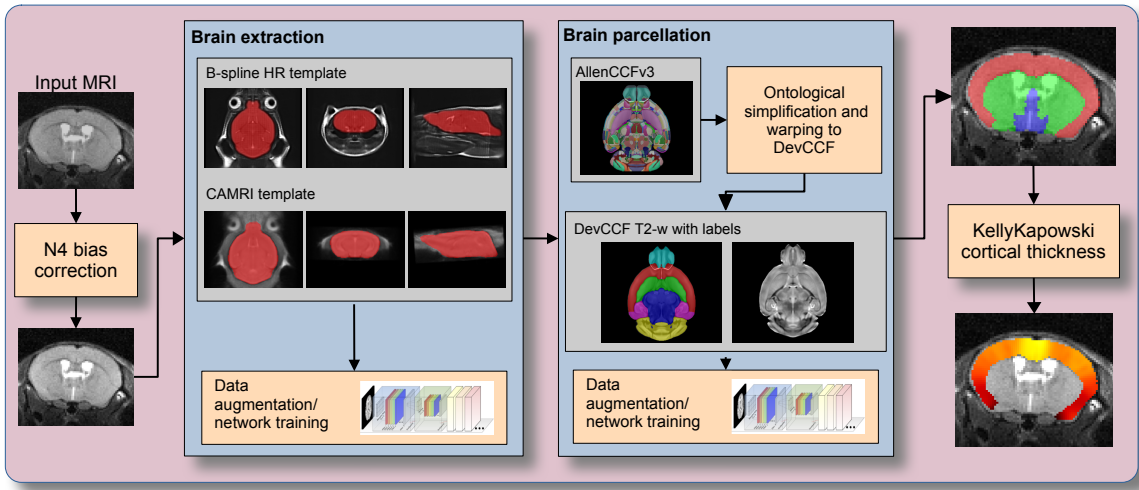


Figure 7: The mouse brain cortical thickness pipeline integrating two deep learning components for brain extraction and brain parcellation prior to estimating cortical thickness. Both deep learning networks rely heavily on data augmentation on templates built from open data and provide an outline for further refinement and creating alternative parcellations for tailored research objectives.

309 One of the most well-utilized pipelines in the ANTsX toolkit is the generation of corti-
 310 cal thickness maps in the human brain from T1-weighted MRI. Starting with the novel
 311 Diffeomorphic Registration-based Cortical Thickness (DiReCT) algorithm,⁵⁵ a complete al-
 312 gorithmic workflow was developed for both cross-sectional⁵⁶ and longitudinal⁵⁷ T1-weighted
 313 MR image data. This contribution was later refactored using deep learning²⁶ leveraging the
 314 earlier results⁵⁶ for training data.

315 In the case of the mouse brain, the lack of training data and/or tools to generate training
316 data making analogous algorithmic development difficult. In addition, mouse data is often
317 characterized by unique issues such as frequent anisotropic sampling which are often in sharp
318 contrast to the high resolution resources available within the community, e.g., AllenCCFv3
319 and DevCCF. Using ANTsX and other publicly available data resources, we developed a
320 complete mouse brain structural morphology pipeline as illustrated in Figure 7 and detailed
321 below.

322 2.3.1 Two-shot mouse brain extraction network

323 In order to create a generalized mouse brain extraction network, we built whole-head tem-
324 plates from two publicly available datasets. The Center for Animal MRI (CAMRI) dataset⁵⁸
325 from the University of North Carolina at Chapel Hill consists of 16 T2-weighted MRI volumes
326 of voxel resolution $0.16 \times 0.16 \times 0.16 mm^3$. The second high-resolution dataset⁵⁹ comprises
327 88 specimens each with three spatially aligned canonical views with in-plane resolution of
328 $0.08 \times 0.08 mm^2$ with a slice thickness of $0.5 mm$. These three orthogonal views were used to
329 reconstruct a single high-resolution volume per subject using a B-spline fitting algorithm de-
330 veloped in ANTsX.⁶⁸ From these two datasets, two symmetric isotropic ANTsX templates⁴⁶
331 were generated analogous to the publicly available ANTsX human brain templates used
332 in previous research.⁵⁶ Bias field simulation, intensity histogram warping, noise simulation,
333 random translation and warping, and random anisotropic resampling in the three canoni-
334 cal directions were used for data augmentation in training a T2-weighted brain extraction
335 network.

336 2.3.2 Single-shot mouse brain parcellation network

337 To create the network for generating a brain parcellation consistent with cortical thickness
338 estimation, we used the AllenCCFv3 and the associated `allensdk` Python library. Using
339 `allensdk`, a gross parcellation labeling was generated from the fine Allen CCFv3 labeling
340 which includes the cerebral cortex, cerebral nuclei, brain stem, cerebellum, main olfactory
341 bulb, and hippocampal formation. This labeling was mapped to the P56 component of

³⁴² the DevCCF. Both the T2-w P56 DevCCF and labelings, in conjunction with the data
³⁴³ augmentation described previously for brain extraction, was used to train a brain parcellation
³⁴⁴ network.

³⁴⁵ **2.3.3 Evaluation**

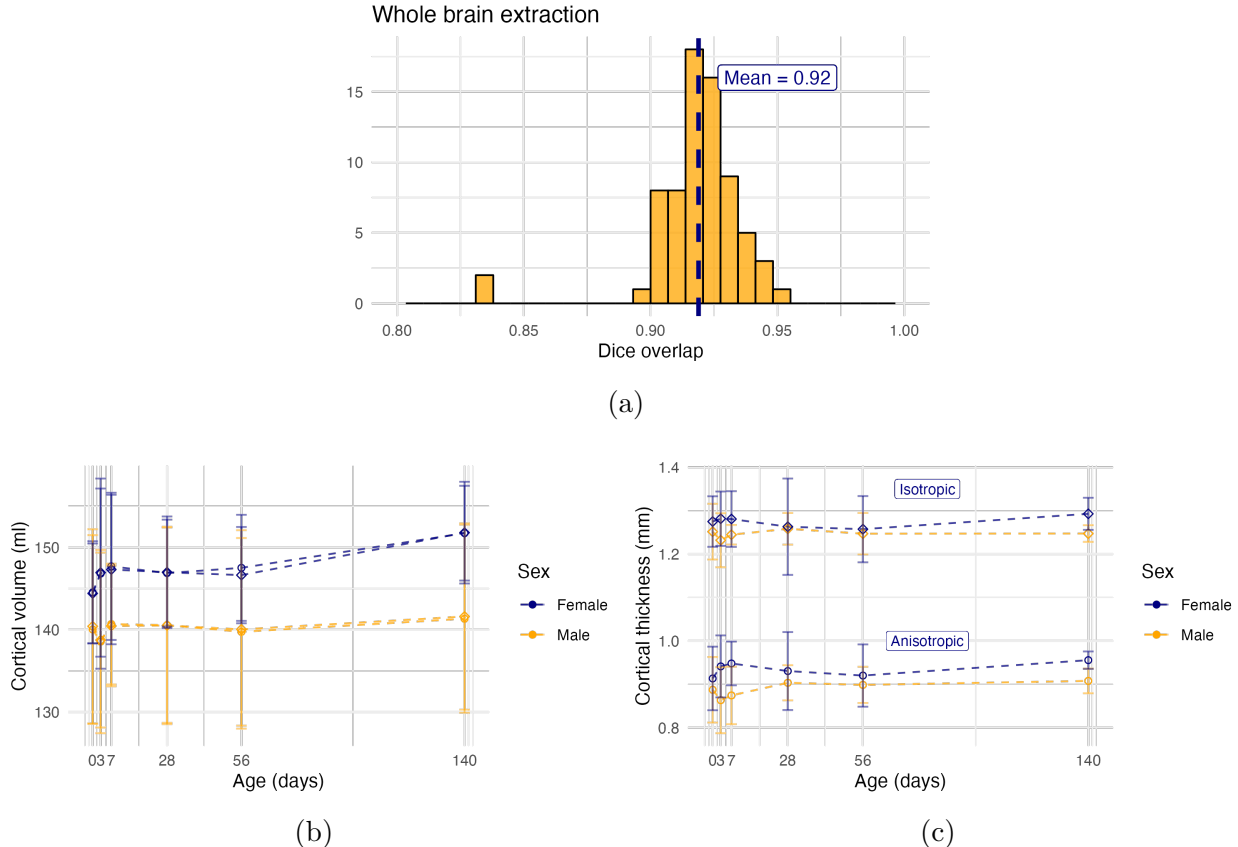


Figure 8: Evaluation of the ANTsX mouse brain extraction, parcellation, and cortical thickness pipeline on an independent dataset consisting of 12 specimens \times 7 time points = 84 total images. (a) Dice overlap comparisons with the provided brain masks provide generally good agreement with the brain extraction network. (b) Cortical volume measurements show similar average quantities over growth and development between the original anisotropic data and interpolated isotropic data. (c) These results contrast with the cortical thickness measurements which show that cortical thickness estimation in anisotropic space severely underestimates the actual values.

³⁴⁶ For evaluation, we used an additional publicly available dataset⁶⁰ which is completely in-
³⁴⁷ dependent from the data used in training the brain extraction and parcellation networks.
³⁴⁸ Data includes 12 specimens each imaged at seven time points (Day 0, Day 3, Week 1, Week

³⁴⁹ 4, Week 8, Week 20) with available brain masks. In-plane resolution is $0.1 \times 0.1 mm^2$ with
³⁵⁰ a slice thickness of $0.5 mm$. Since the training data is isotropic and data augmentation in-
³⁵¹ cludes downsampling in the canonical directions, each of the two networks learns mouse
³⁵² brain-specific interpolation such that one can perform prediction on thick-sliced images, as,
³⁵³ for example, in these evaluation data, and return isotropic probability and thickness maps (a
³⁵⁴ choice available to the user). Figure 8 summarizes the results of the evaluation and compar-
³⁵⁵ ison between isotropic and anisotropic cortical measurements in male and female specimens.

356 **3 Discussion**

357 The ANTsX ecosystem is a powerful framework that has demonstrated applicability to mul-
358 tiple species and organ systems, including the mouse brain. This is further evidenced by the
359 many software packages that use various ANTsX components in their own mouse-specific
360 workflows. In and of itself, the extensive functionality of ANTsX makes it possible to create
361 complete processing pipelines without requiring the integration of multiple packages. These
362 open-source components not only perform well but are available across multiple platforms
363 which facilitates the construction of tailored pipelines for individual study solutions. These
364 components are also supported by years of development not only by the ANTsX development
365 team but by the larger ITK community.

366 In the case of the development of the DevCCF, ANTsX was crucial in providing necessary
367 functionality for yielding high quality output. For the generation of the individual develop-
368 mental stage multi-modal, symmetric templates, ANTsX is unique amongst image analysis
369 software packages in providing existing solutions for template generation which have been
370 thoroughly vetted, including being used in several studies over the years, and which continue
371 to be under active refinement. At its core, computationally efficient and quality template
372 generation requires the use of precision pairwise image mapping functionality which, histori-
373 cally, is at the origins of the ANTsX ecosystem. Moreover, these mapping capabilities extend
374 beyond template generation to the mapping of other image data (e.g., gene expression maps)
375 to a selected template for providing further insight into the mouse brain.

376 With respect to the DevCCF, despite the significant expansion of available developmental age
377 templates beyond what existed previously, there are still temporal gaps in the DevCCF which
378 can be potentially sampled by future research efforts. However, pioneering work involving
379 time-varying diffeomorphic transformations allow us to continuously situate the existing
380 templates within a velocity flow model. This allows one to determine the diffeomorphic
381 transformation from any one temporal location to any other temporal location within the
382 time span defined by the temporal limits of the DevCCF. This functionality is built on
383 multiple ITK components including the B-spline scattered data approximation technique for
384 field regularization and velocity field integration. This velocity field model permits intra-

³⁸⁵ template comparison and the construction of virtual templates where a template can be
³⁸⁶ estimated at any continuous time point within the temporal domain. This novel application
³⁸⁷ can potentially enhance our understanding of intermediate developmental stages.

³⁸⁸ We also presented a mouse brain pipeline for brain extraction, parcellation, and cortical
³⁸⁹ thickness using single-shot and two-shot learning with data augmentation. This approach
³⁹⁰ attempts to circumvent (or at least minimize) the typical requirement of large training
³⁹¹ datasets as with the human ANTsX pipeline analog. However, even given our initial success
³⁹² on independent data, we fully anticipate that refinements will be necessary. Given that the
³⁹³ ANTsX toolkit is a dynamic effort undergoing continual improvement, we manually correct
³⁹⁴ cases that fail and use them for future training and refinement of network weights as we have
³⁹⁵ done for our human-based networks. Generally, these approaches provide a way to bootstrap
³⁹⁶ training data for manual refinement and future generation of more accurate deep learning
³⁹⁷ networks in the absence of other applicable tools.

398 **4 Methods**

399 The following methods are all available as part of the ANTsX ecosystem with analogous
400 elements existing in both ANTsR (ANTs in R) and ANTsPy (ANTs in Python) with an
401 ANTs/ITK C++ core. However, most of the development for the work described below was
402 performed using ANTsPy. For equivalent calls in ANTsR, please see the ANTsX tutorial at
403 <https://tinyurl.com/antsxtutorial>.

404 **4.1 General ANTsX utilities**

405 **4.1.1 Preprocessing: bias field correction and denoising**

406 Bias field correction and image denoising are standard preprocessing steps in improving over-
407 all image quality in mouse brain images. The bias field, a gradual spatial intensity variation
408 in images, can arise from various sources such as magnetic field inhomogeneity or acquisition
409 artifacts, leading to distortions that can compromise the quality of brain images. Correct-
410 ing for bias fields ensures a more uniform and consistent representation of brain structures,
411 enabling more accurate quantitative analysis. Additionally, brain images are often suscep-
412 tible to various forms of noise, which can obscure subtle features and affect the precision
413 of measurements. Denoising techniques help mitigate the impact of noise, enhancing the
414 signal-to-noise ratio and improving the overall image quality. The well-known N4 bias field
415 correction algorithm²⁵ has its origins in the ANTs toolkit which was implemented and intro-
416 duced into the ITK toolkit, i.e. `ants.n4_bias_field_correction(...)`. Similarly, ANTsX
417 contains an implementation of a well-performing patch-based denoising technique⁴⁸ and is
418 also available as an image filter to the ITK community, `ants.denoise_image(...)`.

419 **4.1.2 Image registration**

420 The ANTs registration toolkit is a complex framework permitting highly tailored solu-
421 tions to pairwise image registration scenarios.⁶⁹ It includes innovative transformation mod-
422 els for biological modeling^{42,54} and has proven capable of excellent performance.^{43,70} Var-

423 ious parameter sets targeting specific applications have been packaged with the different
424 ANTsX packages, specifically ANTs, ANTsPy, and ANTsR.²⁶ In ANTsPy, the function
425 `ants.registration(...)` is used to register a pair of images or a pair of image sets where
426 `type_of_transform` is a user-specified option that invokes a specific parameter set. For ex-
427 ample `type_of_transform='antsRegistrationSyNQuick[s]`' encapsulates an oft-used pa-
428 rameter set for quick registration whereas `type_of_transform='antsRegistrationSyN[s]`'
429 is a more detailed alternative. Transforming images using the derived transforms is performed
430 via the `ants.apply_transforms(...)` function.

431 Initially, linear optimization is initialized with center of (intensity) mass alignment typically
432 followed by optimization of both rigid and affine transforms using the mutual information
433 similarity metric. This is followed by diffeomorphic deformable alignment using symmetric
434 normalization (SyN) with Gaussian⁴² or B-spline regularization⁵⁴ where the forward trans-
435 form is invertible and differentiable. The similarity metric employed at this latter stage is
436 typically either neighborhood cross-correlation or mutual information. Note that these pa-
437 rameter sets are robust to input image type (e.g., light sheet fluorescence microscopy, Nissl
438 staining, and the various MRI modalities) and are adaptable to mouse image geometry and
439 scaling. Further details can be found in the various documentation sources for these ANTsX
440 packages.

441 4.1.3 Template generation

442 ANTsX provides functionality for constructing templates from a set (or multi-modal sets) of
443 input images as originally described⁴⁶ and recently used to create the DevCCF templates.¹⁵
444 An initial template estimate is constructed from an existing subject image or a voxelwise
445 average derived from a rigid pre-alignment of the image population. Pairwise registration
446 between each subject and the current template estimate is performed using the Symmetric
447 Normalization (SyN) algorithm.⁴² The template estimate is updated by warping all subjects
448 to the space of the template, performing a voxelwise average, and then performing a “shape
449 update” of this latter image by warping it by the average inverse deformation, thus yielding
450 a mean image of the population in terms of both intensity and shape. The corresponding

451 ANTsPy function is `ants.build_template(...)`.

452 4.1.4 Visualization

453 To complement the well-known visualization capabilities of R and Python, e.g., `ggplot2`
454 and `matplotlib`, respectively, image-specific visualization capabilities are available in the
455 `ants.plot(...)` function (Python). These are capable of illustrating multiple slices in
456 different orientations with other image overlays and label images.

457 4.2 Mapping fMOST data to AllenCCFv3

458 4.2.1 Preprocessing

- 459 • *Downsampling.* The first challenge when mapping fMOST images into the AllenCCFv3
460 is addressing the resolution scale of the data. Native fMOST data from an individual
461 specimen can range in the order of terabytes, which leads to two main problems. First,
462 volumetric registration methods (particularly those estimating local deformation) have
463 high computational complexity and typically cannot operate on such high-resolution
464 data under reasonable memory and runtime constraints. Second, the resolution of
465 the AllenCCFv3 atlas is much lower than the fMOST data, thus the mapping process
466 will cause much of the high-resolution information in the fMOST images to be lost
467 regardless. Thus, we perform a cubic B-spline downsampling of the fMOST data to
468 reduce the resolution of each image to match the isotropic $25 \mu\text{m}$ voxel resolution of the
469 AllenCCFv3 intensity atlas using `ants.resample_image(...)`. An important detail
470 to note is that while the fMOST images and atlas are downsampled, the mapping
471 learned during the registration is assumed to be continuous. Thus, after establishing
472 the mapping to the AllenCCFv3, we can interpolate the learned mapping and apply it
473 directly to the high-resolution native data directly to transform any spatially aligned
474 data (such as the single-cell neuron reconstructions) into the AllenCCFv3.

- 475 • *Stripe artifact removal.* Repetitive pattern artifacts are a common challenge in fMOST
476 imaging where inhomogeneity during the cutting and imaging of different sections can

477 leave stripes of hyper- and hypo-intensity across the image. These stripe artifacts
478 can be latched onto by the registration algorithm as unintended features that are
479 then misregistered to non-analogous structures in the AllenCCFv3. We address these
480 artifacts by fitting a 3-D bandstop (notch) filter to target the frequency of the stripe
481 patterns and removing them prior to the image registration.

- 482 • *Inhomogeneity correction.* Regional intensity inhomogeneity can also occur within
483 and between sections in fMOST imaging due to staining or lighting irregularity during
484 acquisition. Similar to stripe artifacts, intensity gradients due to inhomogeneity
485 can be misconstrued as features during the mapping and result in matching of non-
486 corresponding structures. Our pipeline addresses these intensity inhomogeneities using
487 N4 bias field correction,²⁵ `ants.n4_bias_field_correction(...)`.

488 **4.2.2 Steps for spatial normalization to AllenCCFv3**

- 489 1. *Average fMOST atlas as an intermediate target.* Due to the preparation of the mouse
490 brain for fMOST imaging, the resulting structure in the mouse brain has several large
491 morphological deviations from the AllenCCFv3 atlas. Most notable of these is an en-
492 largement of the ventricles, and compression of cortical structures. In addition, there is
493 poor intensity correspondence for the same anatomic features due to intensity dissim-
494 ilarity between imaging modalities. We have found that standard intensity-base reg-
495 istration is insufficient to capture the significant deformations required to map these
496 structures correctly into the AllenCCFv3. We address this challenge in ANTsX by
497 using explicitly corresponding parcellations of the brain, ventricles and surrounding
498 structures to directly recover these large morphological differences. However, generat-
499 ing these parcellations for each individual mouse brain is a labor-intensive task. Our
500 solution is to create an average atlas whose mapping to AllenCCFv3 encapsulates these
501 large morphological differences to serve as an intermediate registration point. This has
502 the advantage of only needing to generate one set of corresponding annotations which
503 is used to register between the two atlas spaces. New images are first aligned to the
504 fMOST average atlas, which shares common intensity and morphological features and

505 thus can be achieved through standard intensity-based registration.

- 506 2. *Average fMOST atlas construction.* An intensity and shape-based contralaterally sym-
507 metric average of the fMOST image data is constructed from 30 images and their
508 contralateral flipped versions. We ran three iterations of the atlas construction using
509 the default settings. Additional iterations (up to six) were evaluated and showed mini-
510 mal changes to the final atlas construction, suggesting a convergence of the algorithm.
- 511 3. *fMOST atlas to AllenCCFv3 alignment.* Alignment between the fMOST average atlas
512 and AllenCCFv3 was performed using a one-time annotation-driven approach. Label-
513 to-label registration is used to align 7 corresponding annotations in both atlases in
514 the following: 1) brain mask/ventricles, 2) caudate/putamen, 3) fimbria, 4) posterior
515 choroid plexus, 5) optic chiasm, 6) anterior choroid plexus, and 7) habenular com-
516 missure. The alignments were performed sequentially, with the largest, most relevant
517 structures being aligned first using coarse registration parameters, followed by other
518 structures using finer parameters. This coarse-to-fine approach allows us to address
519 large morphological differences (such as brain shape and ventricle expansion) at the
520 start of registration and then progressively refine the mapping using the smaller struc-
521 tures. The overall ordering of these structures was determined manually by an expert
522 anatomist, where anatomical misregistration after each step of the registration was
523 evaluated and used to determine which structure should be used in the subsequent it-
524 eration to best improve the alignment. The transformation from this one-time expert-
525 guided alignment is preserved and used as the canonical fMOST atlas to AllenCCFv3
526 mapping in the pipeline.
- 527 4. *Alignment of individual fMOST mouse brains.* The canonical transformation between
528 the fMOST atlas and AllenCCFv3 greatly simplifies the registration of new individ-
529 ual fMOST mouse brains into the AllenCCFv3. Each new image is first registered
530 into the fMOST average atlas, which shares intensity, modality, and morpholog-
531 ical characteristics. This allows us to leverage standard, intensity-based registration
532 functionality⁶⁹ available in ANTsX to perform this alignment. Transformations are
533 then concatenated to the original fMOST image to move it into the AllenCCFv3 space

534 using ants.apply_transforms(...).

- 535 5. *Transformation of single cell neurons.* A key feature of fMOST imaging is the ability
536 to reconstruct and examine whole-brain single neuron projections⁶⁴. Spatial mapping
537 of these neurons from individual brains into the AllenCCFv3 allows investigators to
538 study different neuron types within the same space and characterize their morphology
539 with respect to their transcriptomics. Mappings found between the fMOST image
540 and the AllenCCFv3 using our pipeline can be applied in this way to fMOST neuron
541 reconstruction data.

542 **4.3 Mapping MERFISH data to AllenCCFv3**

543 **4.3.1 Preprocessing**

- 544 • *Initial volume reconstruction.* Alignment of MERFISH data into a 3-D atlas space
545 requires an estimation of anatomical structure within the data. For each section,
546 this anatomic reference image was created by aggregating the number of detected
547 genetic markers (across all probes) within each pixel of a $10 \times 10\mu m^2$ grid to match
548 the resolution of the $10\mu m$ AllenCCFv3 atlas. These reference image sections are then
549 coarsely reoriented and aligned across sections using manual annotations of the most
550 dorsal and ventral points of the midline. The procedure produces an anatomic image
551 stack that serves as an initialization for further global mappings into the AllenCCFv3.
552 • *Anatomical correspondence labeling.* Mapping the MERFISH data into the AllenCCFv3
553 requires us to establish correspondence between the anatomy depicted in the MERFISH
554 and AllenCCFv3 data. Intensity-based features in MERFISH data are not sufficiently
555 apparent to establish this correspondence, so we need to generate instead corresponding
556 anatomical labelings of both images with which to drive registration. These labels are
557 already available as part of the AllenCCFv3; thus, the main challenge is deriving
558 analogous labels from the spatial transcriptomic maps of the MERFISH data. Toward
559 this end, we assigned each cell from the scRNA-seq dataset to one of the following
560 major regions: cerebellum, CTXsp, hindbrain, HPF, hypothalamus, isocortex, LSX,

midbrain, OLF, PAL, sAMY, STRd, STRv, thalamus and hindbrain. A label map of each section was generated for each region by aggregating the cells assigned to that region within a $10 \times 10\mu\text{m}^2$ grid. The same approach was used to generate more fine grained region specific landmarks (i.e., cortical layers, habenula, IC). Unlike the broad labels which cover large swaths of the section these regions are highly specific to certain parts of the section. Once cells in the MERFISH data are labeled, morphological dilation is used to provide full regional labels for alignment into the AllenCCFv3.

- *Section matching.* Since the MERFISH data is acquired as sections, its 3-D orientation may not be fully accounted for during the volume reconstruction step, due to the particular cutting angle. This can lead to obliqueness artifacts in the section where certain structures can appear to be larger or smaller, or missing outright from the section. To address this, we first use a global alignment to match the orientations of the MERFISH sections to the atlas space. In our pipeline, this section matching is performed in the reverse direction by performing a global affine transformation of the AllenCCFv3 into the MERFISH data space, and then resampling digital sections from the AllenCCFv3 to match each MERFISH section. This approach limits the overall transformation and thus resampling that is applied to the MERFISH data, and, since the AllenCCFv3 is densely sampled, it also reduces in-plane artifacts that result from missing sections or undefined spacing in the MERFISH data.

4.3.2 2.5D deformable, landmark-driven alignment to AllenCCFv3

After global alignment of the AllenCCFv3 into the MERFISH dataset, 2D per-section deformable refinements are used to address local differences between the MERFISH sections and the resampled AllenCCFv3 sections. Nine registrations were performed in sequence using a single label at each iteration in the following order: 1) brain mask, 2) isocortex (layer 2+3), 3) isocortex (layer 5), 4) isocortex (layer 6), 5) striatum, 6) medial habenula, 7) lateral habenula, 8) thalamus, and 9) hippocampus. This ordering was determined empirically by an expert anatomist who prioritized which structure to use in each iteration by evaluating the anatomical alignment from the previous iteration. Global and local mappings are

589 then all concatenated (with appropriate inversions) to create the final mapping between the
590 MERFISH data and AllenCCFv3. This mapping is then used to provide a point-to-point
591 correspondence between the original MERFISH coordinate space and the AllenCCFv3 space,
592 thus allowing mapping of individual genes and cell types located in the MERFISH data to
593 be directly mapped into the AllenCCFv3.

594 4.4 DevCCF velocity flow transformation model

595 Given multiple, linearly or non-linearly ordered point sets where individual points across the
596 sets are in one-to-one correspondence, we developed an approach for generating a velocity
597 flow transformation model to describe a time-varying diffeomorphic mapping as a variant of
598 the landmark matching solution. Integration of the resulting velocity field can then be used
599 to describe the displacement between any two time points within this time-parameterized
600 domain. Regularization of the sparse correspondence between point sets is performed using
601 a generalized B-spline scattered data approximation technique,⁶⁸ also created by the ANTsX
602 developers and contributed to ITK.

603 4.4.1 Velocity field optimization

604 To apply this methodology to the developmental templates,¹⁵ we coalesced the manual an-
605 notations of the developmental templates into 26 common anatomical regions (see Figure 3).
606 We then used these regions to generate invertible transformations between successive time
607 points. Specifically each label was used to create a pair of single region images resulting in 26
608 pairs of “source” and “target” images. The multiple image pairs were simultaneously used to
609 iteratively estimate a diffeomorphic pairwise transform. Given the seven atlases E11.5, E13.5,
610 E15.5, E18.5, P4, P14, and P56, this resulted in 6 sets of transforms between successive time
611 points. Approximately 10^6 points were randomly sampled labelwise in the P56 template
612 space and propagated to each successive atlas providing the point sets for constructing the
613 velocity flow model. Approximately 125 iterations resulted in a steady convergence based
614 on the average Euclidean norm between transformed point sets. Ten integration points were

615 used and point sets were distributed along the temporal dimension using a log transform for
616 a more evenly spaced sampling. For additional information a help menu is available for the
617 ANTsPy function `ants.fit_time_varying_transform_to_point_sets(...)`.

618 4.5 ANTsXNet mouse brain applications

619 4.5.1 General notes regarding deep learning training

620 All network-based approaches described below were implemented and organized in the
621 ANTsXNet libraries comprising Python (ANTsPyNet) and R (ANTsRNet) analogs using
622 the Keras/Tensorflow libraries available as open-source in ANTsX GitHub repositories.
623 For the various applications, both share the identically trained weights for mutual re-
624 producibility. For all GPU training, we used Python scripts for creating custom batch
625 generators which we maintain in a separate GitHub repository for public availability
626 (<https://github.com/ntustison/ANTsXNetTraining>). These scripts provide details such as
627 batch size, choice of loss function, and network parameters. In terms of GPU hardware, all
628 training was done on a DGX (GPUs: 4X Tesla V100, system memory: 256 GB LRDIMM
629 DDR4).

630 Data augmentation is crucial for generalizability and accuracy of the trained networks.
631 Intensity-based data augmentation consisted of randomly added noise (i.e., Gaussian, shot,
632 salt-and-pepper), simulated bias fields based on N4 bias field modeling, and histogram warp-
633 ing for mimicking well-known MRI intensity nonlinearities.^{26,71} These augmentation tech-
634 niques are available in ANTsXNet (only ANTsPyNet versions are listed with ANTsRNet
635 versions available) and include:

- 636 • image noise: `ants.add_noise_to_image(...)`,
- 637 • simulated bias field: `antspynet.simulate_bias_field(...)`, and
- 638 • nonlinear intensity warping: `antspynet.histogram_warp_image_intensities(...)`.

639 Shape-based data augmentation used both random linear and nonlinear deformations in
640 addition to anisotropic resampling in the three canonical orientations to mimic frequently
641 used acquisition protocols for mice brains:

- 642 • random spatial warping: `antspynet.randomly_transform_image_data(...)` and
643 • anisotropic resampling: `ants.resample_image(...)`.

644 **4.5.2 Brain extraction**

645 Similar to human neuroimage processing, brain extraction is a crucial preprocessing step
646 for accurate brain mapping. We developed similar functionality for T2-weighted mouse
647 brains. This network uses a conventional U-net architecture⁷² and, in ANTsPyNet, this
648 functionality is available in the program `antspynet.mouse_brain_extraction(...)`.
649 For the two-shot T2-weighted brain extraction network, two brain templates were gen-
650 erated along with their masks. One of the templates was generated from orthogonal
651 multi-plane, high resolution data⁵⁹ which were combined to synthesize isotropic volu-
652 metric data using the B-spline fitting algorithm.⁶⁸ This algorithm is encapsulated in
653 `ants.fit_bspline_object_to_scattered_data(...)` where the input is the set of voxel
654 intensity values and each associated physical location. Since each point can be assigned
655 a confidence weight, we use the normalized gradient value to more heavily weight edge
656 regions. Although both template/mask pairs are available in the GitHub repository
657 associated with this work, the synthesized volumetric B-spline T2-weighted pair is available
658 within ANTsXNet through the calls:

- 659 • template: `antspynet.get_antsxnet_data("bsplineT2MouseTemplate")` and
660 • mask: `antspynet.get_antsxnet_data("bsplineT2MouseTemplateBrainMask")`.

661 **4.5.3 Brain parcellation**

662 The T2-weighted brain parcellation network is also based on a 3-D U-net architecture and the
663 T2-w DevCCF P56 template component with extensive data augmentation, as described pre-

664 viously. Intensity differences between the template and any brain extracted input image are
665 minimized through the use of the rank intensity transform (`ants.rank_intensity(...)`).
666 Shape differences are reduced by the additional preprocessing step of warping the brain ex-
667 tracted input image to the template. Additional input channels include the prior probability
668 images created from the template parcellation. These images are also available through the
669 ANTsXNet `get_antsxnet_data(...)` interface.

670 **Data availability**

671 All data and software used in this work are publicly available. The DevCCF atlas is
672 available at <https://kimlab.io/brain-map/DevCCF/>. ANTsPy, ANTsR, ANTsPyNet, and
673 ANTsRNet are available through GitHub at the ANTsX Ecosystem ([https://github.com/](https://github.com/ANTsX)
674 [ANTsX](#)). Training scripts for all deep learning functionality in ANTsXNet can also be
675 found on GitHub (<https://github.com/ntustison/ANTsXNetTraining>). A GitHub reposi-
676 tory specifically pertaining to the AllenCCFv3 mapping is available at <https://github.com/>
677 [dontminchenit/CCFAAlignmentToolkit](#). For the other two contributions contained in this
678 work, the longitudinal DevCCF mapping and mouse cortical thickness pipeline, we refer the
679 interested reader to <https://github.com/ntustison/ANTsXMouseBrainMapping>.

⁶⁸⁰ **Acknowledgments**

⁶⁸¹ Support for the research reported in this work includes funding from the National Institute
⁶⁸² of Biomedical Imaging and Bioengineering (R01-EB031722) and National Institute of Mental
⁶⁸³ Health (RF1-MH124605 and U24-MH114827).

⁶⁸⁴ **Author contributions**

⁶⁸⁵ N.T., M.C., and J.G. wrote the main manuscript text and figures. M.C., M.K., R.D., S.S.,
⁶⁸⁶ Q.W., L.G., J.D., C.G., and J.G. developed the Allen registration pipelines. N.T. and F.K.
⁶⁸⁷ developed the time-varying velocity transformation model for the DevCCF. N.T. and M.T.
⁶⁸⁸ developed the brain parcellation and cortical thickness methodology. All authors reviewed
⁶⁸⁹ the manuscript.

690 **References**

- 691 1. Keller, P. J. & Ahrens, M. B. Visualizing whole-brain activity and development at
692 the single-cell level using light-sheet microscopy. *Neuron* **85**, 462–83 (2015).
- 693 2. La Manno, G. *et al.* Molecular architecture of the developing mouse brain. *Nature*
694 **596**, 92–96 (2021).
- 695 3. Wen, L. *et al.* Single-cell technologies: From research to application. *Innovation*
696 (*Camb*) **3**, 100342 (2022).
- 697 4. Oh, S. W. *et al.* A mesoscale connectome of the mouse brain. *Nature* **508**, 207–14
698 (2014).
- 699 5. Gong, H. *et al.* Continuously tracing brain-wide long-distance axonal projections in
700 mice at a one-micron voxel resolution. *Neuroimage* **74**, 87–98 (2013).
- 701 6. Li, A. *et al.* Micro-optical sectioning tomography to obtain a high-resolution atlas of
702 the mouse brain. *Science* **330**, 1404–8 (2010).
- 703 7. Ueda, H. R. *et al.* Tissue clearing and its applications in neuroscience. *Nat Rev*
704 *Neurosci* **21**, 61–79 (2020).
- 705 8. Ståhl, P. L. *et al.* Visualization and analysis of gene expression in tissue sections by
706 spatial transcriptomics. *Science* **353**, 78–82 (2016).
- 707 9. Burgess, D. J. Spatial transcriptomics coming of age. *Nat Rev Genet* **20**, 317 (2019).
- 708
- 709 10. MacKenzie-Graham, A. *et al.* A multimodal, multidimensional atlas of the C57BL/6J
710 mouse brain. *J Anat* **204**, 93–102 (2004).
- 711 11. Mackenzie-Graham, A. J. *et al.* Multimodal, multidimensional models of mouse brain.
712 *Epilepsia* **48 Suppl 4**, 75–81 (2007).
- 713 12. Dong, H. W. *Allen reference atlas. A digital color brain atlas of the C57BL/6J male*
714 *mouse.* (John Wiley; Sons, 2008).

- 715 13. Wang, Q. *et al.* The allen mouse brain common coordinate framework: A 3D reference
716 atlas. *Cell* **181**, 936–953.e20 (2020).
- 717 14. Johnson, G. A. *et al.* Waxholm space: An image-based reference for coordinating
718 mouse brain research. *Neuroimage* **53**, 365–72 (2010).
- 719 15. Kronman, F. A. *et al.* Developmental mouse brain common coordinate framework.
720 *bioRxiv* (2023) doi:[10.1101/2023.09.14.557789](https://doi.org/10.1101/2023.09.14.557789).
- 721 16. Oguz, I., Zhang, H., Rumple, A. & Sonka, M. RATS: Rapid automatic tissue segmen-
722 tation in rodent brain MRI. *J Neurosci Methods* **221**, 175–82 (2014).
- 723 17. Sawiak, S. J., Picq, J.-L. & Dhenain, M. Voxel-based morphometry analyses of in
724 vivo MRI in the aging mouse lemur primate. *Front Aging Neurosci* **6**, 82 (2014).
- 725 18. Ashburner, J. SPM: A history. *Neuroimage* **62**, 791–800 (2012).
- 726
- 727 19. Modat, M. *et al.* Fast free-form deformation using graphics processing units. *Comput
728 Methods Programs Biomed* **98**, 278–84 (2010).
- 729 20. Tyson, A. L. *et al.* Accurate determination of marker location within whole-brain
730 microscopy images. *Sci Rep* **12**, 867 (2022).
- 731 21. Pallast, N. *et al.* Processing pipeline for atlas-based imaging data analysis of struc-
732 tural and functional mouse brain MRI (AIDAmri). *Front Neuroinform* **13**, 42 (2019).
- 733 22. Jenkinson, M., Beckmann, C. F., Behrens, T. E. J., Woolrich, M. W. & Smith, S. M.
734 FSL. *Neuroimage* **62**, 782–90 (2012).
- 735 23. Yeh, F.-C., Wedeen, V. J. & Tseng, W.-Y. I. Generalized q-sampling imaging. *IEEE
736 Trans Med Imaging* **29**, 1626–35 (2010).
- 737 24. Jorge Cardoso, M. *et al.* STEPS: Similarity and truth estimation for propagated
738 segmentations and its application to hippocampal segmentation and brain parcelation.
Med Image Anal **17**, 671–84 (2013).

- 739 25. Tustison, N. J. *et al.* N4ITK: Improved N3 bias correction. *IEEE Trans Med Imaging*
740 **29**, 1310–20 (2010).
- 741 26. Tustison, N. J. *et al.* The ANTsX ecosystem for quantitative biological and medical
742 imaging. *Sci Rep* **11**, 9068 (2021).
- 743 27. Goubran, M. *et al.* Multimodal image registration and connectivity analysis for inte-
744 gration of connectomic data from microscopy to MRI. *Nat Commun* **10**, 5504 (2019).
- 745 28. Celestine, M., Nadkarni, N. A., Garin, C. M., Bougacha, S. & Dhenain, M. Sammba-
746 MRI: A library for processing SmAll-MaMmal BrAin MRI data in python. *Front
Neuroinform* **14**, 24 (2020).
- 747 29. Ioanas, H.-I., Marks, M., Zerbi, V., Yanik, M. F. & Rudin, M. An optimized regis-
748 tration workflow and standard geometric space for small animal brain imaging. *Neuro-
image* **241**, 118386 (2021).
- 749 30. Cox, R. W. AFNI: What a long strange trip it's been. *Neuroimage* **62**, 743–7 (2012).
750
- 751 31. Anderson, R. J. *et al.* Small animal multivariate brain analysis (SAMBA) - a high
752 throughput pipeline with a validation framework. *Neuroinformatics* **17**, 451–472
(2019).
- 753 32. Ni, H. *et al.* A robust image registration interface for large volume brain atlas. *Sci
754 Rep* **10**, 2139 (2020).
- 755 33. Jin, M. *et al.* SMART: An open-source extension of WholeBrain for intact mouse
756 brain registration and segmentation. *eNeuro* **9**, (2022).
- 757 34. Fürth, D. *et al.* An interactive framework for whole-brain maps at cellular resolution.
758 *Nat Neurosci* **21**, 139–149 (2018).
- 759 35. Negwer, M. *et al.* FriendlyClearMap: An optimized toolkit for mouse brain mapping
760 and analysis. *Gigascience* **12**, (2022).

- 761 36. Qu, L. *et al.* Cross-modal coherent registration of whole mouse brains. *Nat Methods*
762 **19**, 111–118 (2022).
- 763 37. Klein, S., Staring, M., Murphy, K., Viergever, M. A. & Pluim, J. P. W. Elastix: A
764 toolbox for intensity-based medical image registration. *IEEE Trans Med Imaging* **29**,
196–205 (2010).
- 765 38. Carey, H. *et al.* DeepSlice: Rapid fully automatic registration of mouse brain imaging
766 to a volumetric atlas. *Nat Commun* **14**, 5884 (2023).
- 767 39. Bajcsy, R. & Broit, C. Matching of deformed images. in *Sixth International Conference
768 on Pattern Recognition (ICPR'82)* 351–353 (1982).
- 769 40. Bajcsy, R. & Kovacic, S. Multiresolution elastic matching. *Computer Vision, Graph-
770 ics, and Image Processing* **46**, 1–21 (1989).
- 771 41. Gee, J. C., Reivich, M. & Bajcsy, R. Elastically deforming 3D atlas to match anatom-
772 ical brain images. *J Comput Assist Tomogr* **17**, 225–36 (1993).
- 773 42. Avants, B. B., Epstein, C. L., Grossman, M. & Gee, J. C. Symmetric diffeomorphic
774 image registration with cross-correlation: Evaluating automated labeling of elderly
and neurodegenerative brain. *Med Image Anal* **12**, 26–41 (2008).
- 775 43. Klein, A. *et al.* Evaluation of 14 nonlinear deformation algorithms applied to human
776 brain MRI registration. *Neuroimage* **46**, 786–802 (2009).
- 777 44. Murphy, K. *et al.* Evaluation of registration methods on thoracic CT: The EMPIRE10
778 challenge. *IEEE Trans Med Imaging* **30**, 1901–20 (2011).
- 779 45. Baheti, B. *et al.* The brain tumor sequence registration challenge: Establishing corre-
780 spondence between pre-operative and follow-up MRI scans of diffuse glioma patients.
(2021).
- 781 46. Avants, B. B. *et al.* The optimal template effect in hippocampus studies of diseased
782 populations. *Neuroimage* **49**, 2457–66 (2010).

- 783 47. Avants, B. B., Tustison, N. J., Wu, J., Cook, P. A. & Gee, J. C. An open source
multivariate framework for n-tissue segmentation with evaluation on public data.
Neuroinformatics **9**, 381–400 (2011).
- 784
- 785 48. Manjón, J. V., Coupé, P., Martí-Bonmatí, L., Collins, D. L. & Robles, M. Adaptive
non-local means denoising of MR images with spatially varying noise levels. *J Magn
Reson Imaging* **31**, 192–203 (2010).
- 786
- 787 49. Wang, H. *et al.* Multi-atlas segmentation with joint label fusion. *IEEE Trans Pattern
Anal Mach Intell* **35**, 611–23 (2013).
- 788
- 789 50. Tustison, N. J. *et al.* Optimal symmetric multimodal templates and concatenated
random forests for supervised brain tumor segmentation (simplified) with ANTsR.
Neuroinformatics (2014) doi:[10.1007/s12021-014-9245-2](https://doi.org/10.1007/s12021-014-9245-2).
- 790
- 791 51. Tustison, N. J., Yang, Y. & Salerno, M. Advanced normalization tools for cardiac mo-
tion correction. in *Statistical atlases and computational models of the heart - imaging
and modelling challenges* (eds. Camara, O. *et al.*) vol. 8896 3–12 (Springer Interna-
tional Publishing, 2015).
- 792
- 793 52. McCormick, M., Liu, X., Jomier, J., Marion, C. & Ibanez, L. ITK: Enabling repro-
ducible research and open science. *Front Neuroinform* **8**, 13 (2014).
- 794
- 795 53. Beg, M. F., Miller, M. I., Trouvé, A. & Younes, L. Computing large deformation
metric mappings via geodesic flows of diffeomorphisms. *International Journal of
Computer Vision* **61**, 139–157 (2005).
- 796
- 797 54. Tustison, N. J. & Avants, B. B. Explicit B-spline regularization in diffeomorphic image
registration. *Front Neuroinform* **7**, 39 (2013).
- 798
- 799 55. Das, S. R., Avants, B. B., Grossman, M. & Gee, J. C. Registration based cortical
thickness measurement. *Neuroimage* **45**, 867–79 (2009).
- 800
- 801 56. Tustison, N. J. *et al.* Large-scale evaluation of ANTs and FreeSurfer cortical thickness
measurements. *Neuroimage* **99**, 166–79 (2014).
- 802

- 803 57. Tustison, N. J. *et al.* Longitudinal mapping of cortical thickness measurements: An
804 Alzheimer's Disease Neuroimaging Initiative-based evaluation study. *J Alzheimers
Dis* (2019) doi:[10.3233/JAD-190283](https://doi.org/10.3233/JAD-190283).
- 805 58. Hsu, L.-M. *et al.* CAMRI mouse brain MRI data.
- 806
- 807 59. Reshetnikov, V. *et al.* High-resolution MRI data of brain C57BL/6 and BTBR mice
808 in three different anatomical views.
- 809 60. Rahman, N., Xu, K., Budde, M. D., Brown, A. & Baron, C. A. A longitudinal
810 microstructural MRI dataset in healthy C57Bl/6 mice at 9.4 tesla. *Sci Data* **10**, 94
(2023).
- 811 61. Gong, H. *et al.* High-throughput dual-colour precision imaging for brain-wide connec-
812 tome with cytoarchitectonic landmarks at the cellular level. *Nat Commun* **7**, 12142
(2016).
- 813 62. Wang, J. *et al.* Divergent projection patterns revealed by reconstruction of individual
814 neurons in orbitofrontal cortex. *Neurosci Bull* **37**, 461–477 (2021).
- 815 63. Rotolo, T., Smallwood, P. M., Williams, J. & Nathans, J. Genetically-directed, cell
816 type-specific sparse labeling for the analysis of neuronal morphology. *PLoS One* **3**,
e4099 (2008).
- 817 64. Peng, H. *et al.* Morphological diversity of single neurons in molecularly defined cell
818 types. *Nature* **598**, 174–181 (2021).
- 819 65. Yao, Z. *et al.* A high-resolution transcriptomic and spatial atlas of cell types in the
820 whole mouse brain. *Nature* **624**, 317–332 (2023).
- 821 66. Liu, J. *et al.* Concordance of MERFISH spatial transcriptomics with bulk and single-
822 cell RNA sequencing. *Life Sci Alliance* **6**, (2023).
- 823 67. Stringer, C., Wang, T., Michaelos, M. & Pachitariu, M. Cellpose: A generalist algo-
824 rithm for cellular segmentation. *Nat Methods* **18**, 100–106 (2021).

- 825 68. Tustison, N. J. & Amini, A. A. Biventricular myocardial strains via nonrigid regis-
826 tration of anatomical NURBS model [corrected]. *IEEE Trans Med Imaging* **25**, 94–112
(2006).
- 827 69. Avants, B. B. *et al.* The Insight ToolKit image registration framework. *Front Neu-*
828 *roinform* **8**, 44 (2014).
- 829 70. Avants, B. B. *et al.* A reproducible evaluation of ANTs similarity metric performance
830 in brain image registration. *Neuroimage* **54**, 2033–44 (2011).
- 831 71. Nyúl, L. G., Udupa, J. K. & Zhang, X. New variants of a method of MRI scale
832 standardization. *IEEE Trans Med Imaging* **19**, 143–50 (2000).
- 833 72. Falk, T. *et al.* U-net: Deep learning for cell counting, detection, and morphometry.
834 *Nat Methods* **16**, 67–70 (2019).